Journal of Volcanology and Geothermal Research 472 (2026) 108578

Contents lists available at ScienceDirect

Journal of Volcanology and Geothermal Research

journal homepage: www.journals.elsevier.com/journal-of-volcanology-and-geothermal-research

# High-frequency volcano seismic tremor at Mt. Etna, Italy: Insights from varying seismic-acoustic amplitude ratios

Maurice Weber [a,*], Christopher J. Bean [a], Ivan Lokmer [b], Silvio De Angelis [c,d], Luciano Zuccarello [d,c]

[a] *Dublin Institute for Advanced Studies, Dublin, Ireland*
[b] *University College Dublin, Dublin, Ireland*
[c] *University of Liverpool, Liverpool, UK*
[d] *Instituto Nazionale di Geofisica e Vulcanologia, Sezione di Pisa, Pisa, Italy*

## ARTICLE INFO

*Keywords:*
Volcanoes
Seismic tremor
High spectral frequencies
Driving processes
Seismic-acoustic correlations

## ABSTRACT

We present a comprehensive, high-resolution seismic and acoustic datasets from Mt. Etna, Italy acquired through a large, unprecedented deployment of seismometers and microphones in the summit region during summer 2022, highlighting about 50 rarely reported high-frequency (12–15 Hz), short-duration, minute- to half an hour-long volcanic seismic tremor episodes. These events exhibit variable seismic-acoustic amplitude ratios, implying multiple triggering mechanisms. Evidenced by coincident acoustic signals at different distinct frequencies our analysis suggests that while some tremor occurrences are indirectly associated with degassing processes other examples of high-frequency tremor lack any acoustic counterpart, indicating that vigorous degassing and thus fluid migration might not be a primary driver for tremor generation. We propose that in addition to traditional models requiring fluid movement for tremor generation, quasi-brittle, mesoscale failure within weak edifice material may act as a direct source mechanism radiating high-frequency tremor. This interpretation aligns with prior studies on numerical simulations of seismic event generation in typical low-stiffness volcanic materials as well as laboratory experiments with volcanic samples under stress and helps explain shallow seismic tremor episodes in the absence of acoustic signals.

## 1. Introduction

Seismic tremor is considered a critical parameter for volcano monitoring, able to provide valuable insights into the state of activity at volcanoes (e.g. Konstantinou and Schlindwein (2002) or more recently Salerno et al. (2018)) and considered an important tool to support eruption forecasting (Chardot et al., 2015). Understanding the processes that generate the broad range of tremor signals recorded at volcanoes (Konstantinou and Schlindwein, 2002) is essential; yet, a comprehensive understanding of their source mechanisms remains elusive as many processes are potentially involved (e.g. Salerno et al. (2018)).

In this study we examine high-frequency volcanic tremor (i.e., at frequencies > 10 Hz) with the aim to shed light on rarely investigated frequency ranges. Volcanic tremor is typically found at frequencies between 0.5 and 5 Hz (McNutt, 1992). Due to the close proximity (<1 km) to the source required to detect coherent tremor above 10 Hz, these higher frequency signals > 10 Hz are typically overlooked revwith a few notable exceptions such as Heleno et al. (2006), Matoza and Fee (2014), Reiss et al. (2023). Analysis and location of high-frequency tremor is further complicated by highly complex waveforms lacking phase arrivals (Permana et al., 2019) as well as significant scattering at higher frequencies from the heterogeneous volcanic edifice (Ibanez et al., 2019). Here, we focus on high-frequency tremor signals recorded at Mt. Etna. Dominant tremor frequencies at Mt. Etna are typically reported at ~3 Hz with energy generally concentrated between 0.5 and 5 Hz (Di Lieto et al., 2007). Tremor is almost consistently present at <5 Hz, even during periods of relative quiescence (no eruptive activity but ongoing degassing). Such tremor is widely interpreted as related to subsurface fluid migration even though analysis is difficult due to significant path effects (Di Lieto et al., 2007; Bean et al., 2013). Except for a few notable studies (e.g., Cannata et al. (2010)) little investigation has been carried out on tremor at frequencies > 10 Hz at Mt. Etna.

This lack of coverage motivates this study where we focus on rarely investigated high frequency ranges attempting to shed further

---

[*] Corresponding author.
*E-mail addresses:* mweber@cp.dias.ie (M. Weber), chris.bean@dias.ie (C.J. Bean), ivan.lokmer@ucd.ie (I. Lokmer), silvioda@liverpool.ac.uk (S.D. Angelis), luciano.zuccarello@ingv.it (L. Zuccarello).

https://doi.org/10.1016/j.jvolgeores.2026.108578
Received 29 September 2025; Received in revised form 16 February 2026; Accepted 22 February 2026

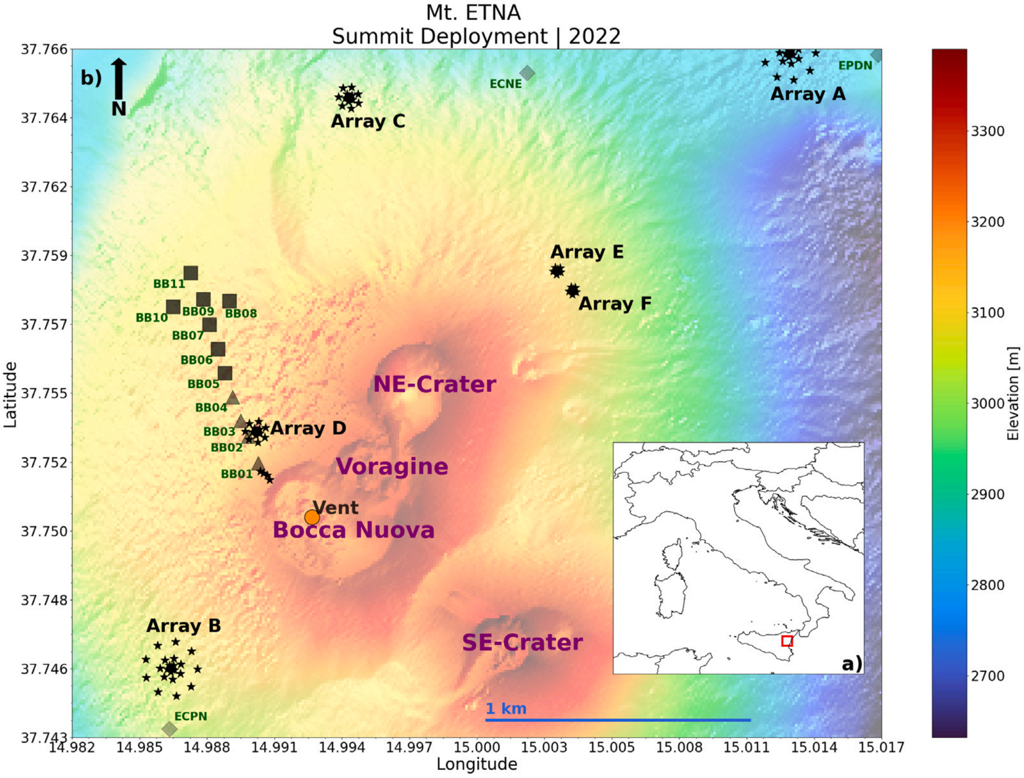

**Fig. 2.1.** All stations deployed during both campaigns to Mt. Etna during summer 2022 seen in Panel (b) with an indication of the location of Mt. Etna in panel (a). All short-period stations are represented by stars, installed in six circular Arrays (A–F) as well as near the BNC. In addition, a linear array of broadband stations (BB01-BB04) and 7 infrasound stations (BB05-BB11) were deployed in an north-north-western direction leading away from BNC. Three stations (ECPN, ECNE, EPDN) of the permanent network operated by Instituto Nazionale di Geofisica e Vulcanologia (INGV) are also indicated.

light on the complex underlying mechanisms behind volcanic tremor exploring seismic-acoustic amplitude ratios and their variability similar to approaches by Matoza and Fee (2014).

## 2. Data

Two campaigns were conducted within the summit region of Mt. Etna during the summer of 2022. These campaigns involved the deployment of six arrays of short-period seismometers (SMARTSOLO nodes, 5 Hz) with approximately circular geometry, each comprising between 9 and 25 instruments. In addition, a linear array including 4 broadband seismometers (Guralp, 60$s$-50 Hz) and 7 infrasound sensors (Nanometrics, Trillium Compact 120$s$) was installed. During the first campaign, in July 2022, the linear array was installed, which remained operational for 50 days. Later, during the second campaign, between 25th August and 1st September, the circular arrays (SMARTSOLO nodes, 5 Hz) were deployed and the linear array was extended towards the Bocca Nuova Crater (BNC) with the addition of 4 short-period stations (SMARTSOLO nodes, 5 Hz).

This deployment was unprecedented at Etna for its size, station density and coverage of the summit area, and particularly well-suited for the investigation of high-frequency tremor above 10 Hz. A map showing the distribution of stations is found in Fig. 2.1 plotted on the Digital Elevation Map after Ganci et al. (2023).

The circular arrays were designed to capture a broad range of frequencies. This was achieved by constructing up to four concentric rings of instruments around a central element with the radius of these rings increasing from only 5 $m$ for the innermost ring to 100 $m$ for the outermost ring, resulting in a maximum aperture of 200 $m$. While the inner ring only consisted of 3 stations the outer one was made up of 9 stations amounting to 25 stations in total. The varying radius of the rings and range of inter-station distances allowed an array response 1–5 Hz and up to ~ 100 Hz (see Fig. 2.2). Even though the SMARTSOLO nodes' response begins to fall off at 5 Hz the instrument's sensitivity is sufficient down to $<$ 1 Hz which is still covered by the array's response. Similarly, the upper end of the response matches the Nyquist-frequency at 125 Hz. Our main frequency band of interest is 10–20 Hz and therefore well covered by the array configuration. With 104 short-period stations available in total, two arrays were constructed with the full 25-station configuration (2.1, Arrays A and B) as described while the remaining arrays were scaled down. Two arrays were missing the outer ring of 9 stations (Arrays C and D), which reduced the number of stations in those arrays to 16 with a maximum aperture of 80 $m$, while for the remaining two arrays (E and F) the third ring consisting of 7 stations was also removed leaving just 9 stations and a maximum aperture of only 30 $m$.

The locations of the arrays were significantly constrained by accessibility within the summit region. Two arrays were installed in close proximity to BNC (Arrays B and D), one of which (Array D) was co-located with a broadband station of the linear profile, while other two were installed near the North-East Crater (NEC) providing full coverage of the central summit craters. A large section around the South-East Crater (SEC) was not accessible; thus, the remaining two arrays were deployed at slightly larger distance from the summit in the North and Northeast direction. The most interesting results were obtained by the two arrays B and D and linear array closest to BNC.

## 3. Episodic high-frequency tremor near the summit craters

The geometry of our arrays, and their proximity to the summit craters, is geared towards detection of tremor signals at frequencies of 10–20 Hz (Fig. 2.2). We detected several occurrences of rarely observed tremor at approximately 12–15 Hz appearing in short-duration episodes, lasting minutes to about half an hour each (see Fig. 3.1).

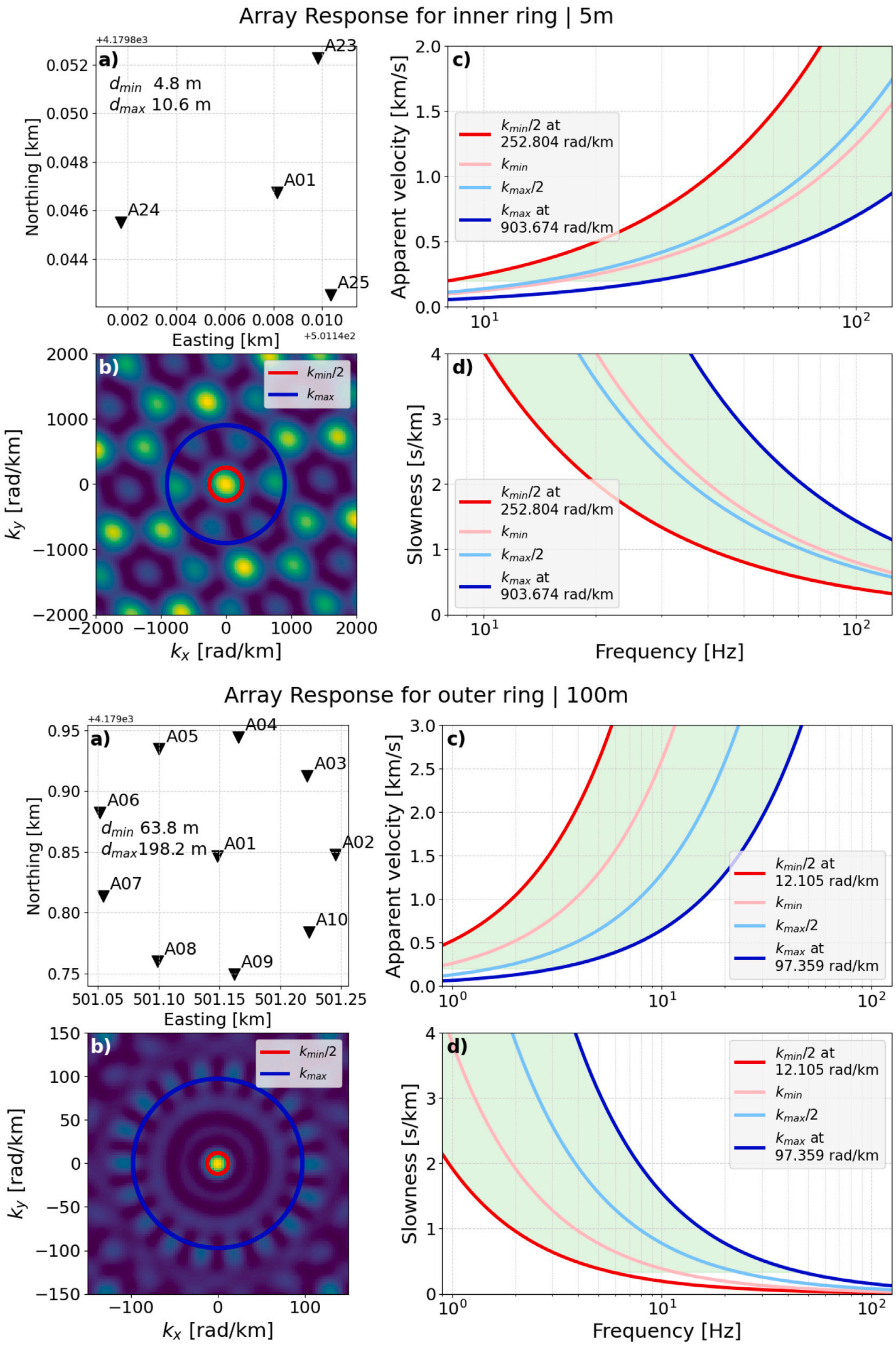

**Fig. 2.2.** Array response for the smallest and largest rings of 5 *m* and 100 *m* radius, respectively. Panels (a) shows the array configuration. Below, in panels (b) the transfer functions as a function of the wavenumber are found. The range of slownesses/velocities and frequencies that the configurations are sensitive to is highlighted by the bright green area while the dark red and dark blue curves represent the upper and lower limit of the response (panels (c) and (d)). Frequencies $< 5$ Hz can be resolved as well as up to $\sim 100$ Hz.

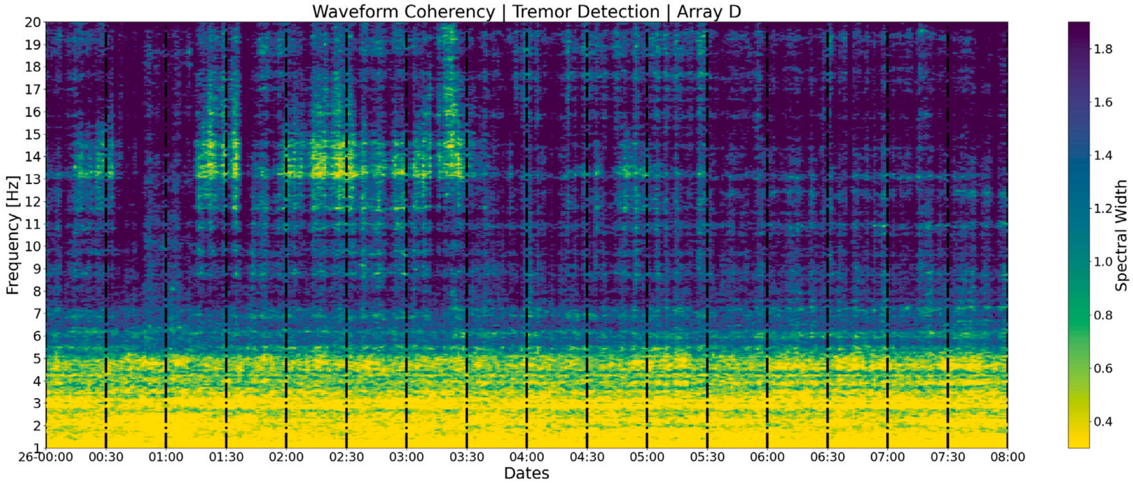

**Fig. 3.1.** 8-hour record starting on 26th August 2022 showing the spectral width (as a measure for waveform coherency) obtained for all 16 short period stations in Array D closest to BNC revealing episodic high-frequency tremor (yellowish patches representing increased coherency most dominant between 13–15 Hz) as well as the typical ever-present Etna-tremor below 5 Hz. The dashed vertical lines mark 30-minute windows.

We use the COVSEISNET tremor detection tool developed by Seydoux et al. (2016), Soubestre et al. (2018), Tong et al. (2024). This approach divides the seismic traces across a network or array into subwindows of which a certain number of adjacent windows are averaged after spectral whitening is applied to the traces. After transforming the signals into the frequency domain, their cross-spectra are calculated between all station combinations yielding the Covariance Matrix of dimensions $N \times N \times f \times t$ where $N$ refers to the number of stations, $f$ to frequency and $t$ to averaged windows in time, respectively. The cross-spectra are calculated on individual subwindows while the Covariance matrix represents the average of all cross-spectra for a certain number of consecutive subwindows.

Fig. 3.1 shows the background low-frequency tremor typically reported at Mt. Etna (Di Lieto et al., 2007) at frequencies below 5 Hz. Very distinctive short-duration episodes of tremor are also visible primarily in the 12–15 Hz band (affecting also adjacent frequencies) until 03:30 emerging from uncorrelated background noise. The episodic nature of the high-frequency signal, in contrast to the continuous appearance of the low-frequency tremor, suggests that their source mechanisms are likely different.

## 4. Time evolution of seismic and acoustic signals

Johnson and Aster (2005) have demonstrated that seismic-acoustic ratios are a highly useful parameter enabling differentiation between various eruption source processes. Similarly, we investigate seismic and acoustic amplitudes here attempting to infer about underlying processes producing seismic tremor episodes during a period of no eruptive activity at Mt. Etna but when continuous degassing was present. Fig. 4.1 shows the temporal evolution of seismic energy in the frequency band 12–15 Hz (Panel (a)). We plot the median amplitudes for non-overlapping 10-minute windows averaging all stations from Array D, the closest to the summit craters (Fig. 2.1). The median amplitudes across the entire deployment are indicated as dashed lines.

There is a long-term trend clearly visible with stronger seismicity registered early which then decreases below the respective means (dashed lines) before gradually increasing again in the second half of the deployment (starting 29th August). This leads up to a second maximum in seismic energy recorded shortly before the instruments were retrieved. There are also significant short-term variations related to bursts or episodes of high-frequency tremor which are strongest near both the beginning and end of the deployment period until 05:00 UTC 26th August and after 00:00 UTC 1st September.

Firstly, we were interested in how the high-frequency tremor band correlates with “typical” tremor at Mt. Etna. In the past, tremor at Mt. Etna has mainly been reported in the band 1–5 Hz (Di Lieto et al., 2007). The temporal evolution of the signal in this band during our deployment is plotted in Panel (b). A very similar long-term trend across the deployment period is clearly noticeable suggesting a potential link between the processes generating seismicity in both frequency bands. Closer inspection though reveals clear differences at shorter time scales. This can be observed from the seismic ratio (12–15 Hz vs. 1–5 Hz, see Panel (e)) - this ratio shows a constant long-term behaviour, however, exhibits strong short-term variations (also note logarithmic $y$-axis scaling). For example, one of the strongest high-frequency tremor episodes recorded between 01:00 and 04:00 in the morning of 26th August is not matched by such high energy levels in the 1–5 Hz band. Similarly, another high-frequency tremor burst found at 20:00 on 30th August is not accompanied by any increase in amplitudes between 1–5 Hz. A mismatch between the two frequency bands is also observed between 22:00 on the 29th and 06:00 on the 30th, when quasi-periodic peaks similar in duration and amplitude are observed in the 1–5 Hz range, but not matched in the 12–15 Hz band. These incidences indicate that tremor at 12–15 Hz is unlikely to be directly triggered by the same source mechanism driving the typical tremor <5 Hz but may be treated as a separate signal, even though a similar long-term trend is found.

As discussed previously, volcanic tremor at Mt. Etna is frequently associated with degassing activity, which would also present an acoustic signature. Even though Mt. Etna’s overall activity was very weak during the deployment both BNC as well as SEC were, in fact, continuously degassing. The temporal evolution of infrasound amplitudes recorded at station BB05, the closest to Array D (Fig. 2.1), is plotted in the Panels (c) and (d). Signal median values for atmospheric pressure are shown for 10-minute windows (purple graphs) filtered between 3–5 Hz and 12–15 Hz bands, respectively, with overall median added as a dashed line. Additionally, the pink graph displays the same data filtered between 15–30 Hz serving as a proxy for potential acoustic noise linked to strong winds and rainfall during the deployment. Infrasound stations were dismantled one day earlier than the seismic stations, hence the gap in acoustic data towards the end of the deployment period after 09:00 UTC 31st August.

The 3–5 Hz band was deemed the most interesting owing to its occasional correlation with high-frequency tremor amplitudes, e.g. we find a high level of acoustic energy accompanying high-frequency tremor, which then decreases significantly as the high-frequency tremor does too (note logarithmic scale in acoustic panel) during the first

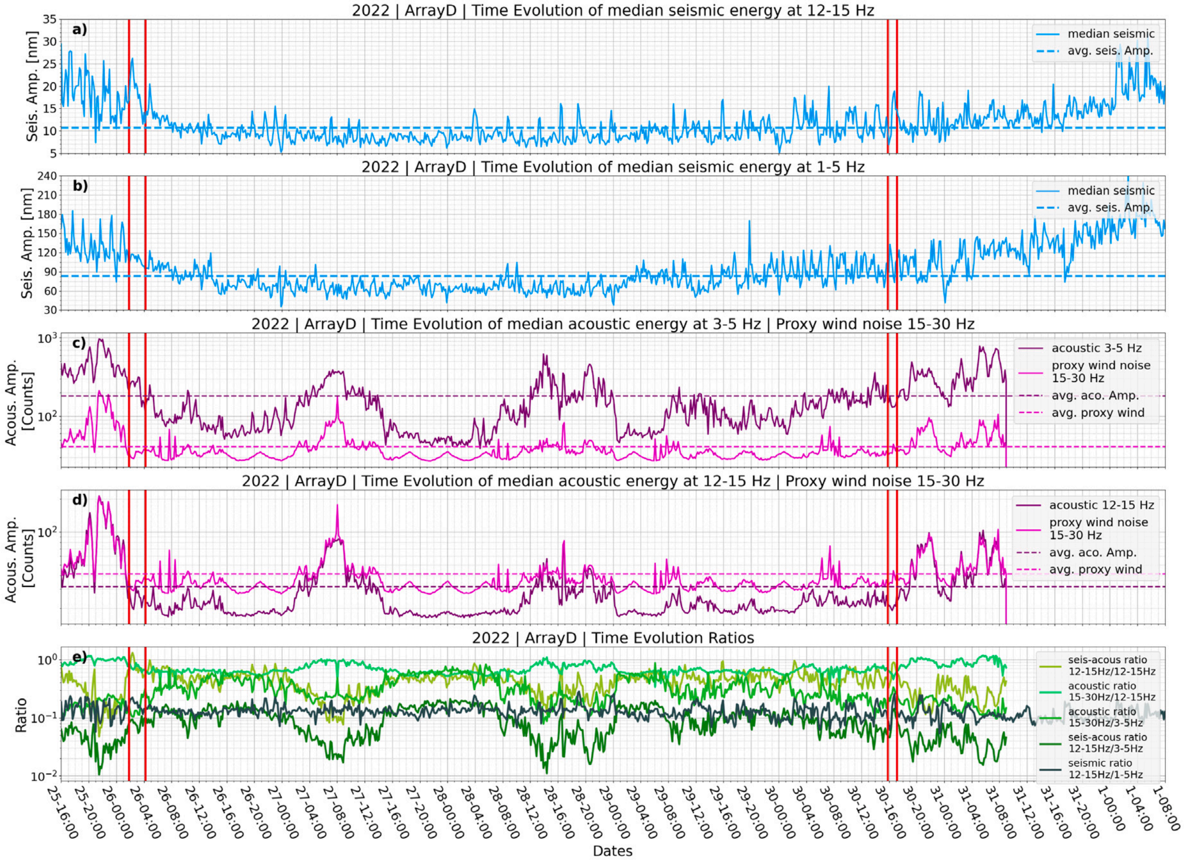

**Fig. 4.1.** Evolution over time for seismic (Panel (a), 12–15 Hz and Panel (b), 1–5 Hz) and acoustic energy (Panel (c), 3–5 Hz and Panel (d), 12–15 Hz) recorded in various frequency bands of interest and their ratios (Panel (e)) during the entire short period instrument deployment for all stations of Array D. Two sections are marked by red vertical lines in panel (a) which are closely investigated in Figs. 5.1, 5.3 and 5.4.

window of interest between 02:00 and 04:00 on 26th August. The occasional character of this relationship is seen in the later window of interest between 16:00 and 17:00 on 30th August when the acoustic energy shows no increase during the tremor episode.

Acoustic energy increases gradually during the second half of the deployment similar to the seismic amplitudes. It should be noted though, that especially between 20:00 on 25th August and midnight acoustic energy levels are very high across broad ranges indicated by the red curve suggesting that atmospheric disturbances may have contributed to the very high amplitude level at 3–5 Hz at that time. On the other hand, we find two more periods (02:00 to 14:00 on 27th and 08:00 to midnight on 28th August) of increased acoustic energy at 3–5 Hz. However, these two periods do not coincide with increased seismic amplitudes similar to those towards the beginning and end of the deployment. While the period between 05:00 and 10:00 on 27th August may also be affected by weather conditions as noise increases significantly between 15–30 Hz the other before-mentioned period on 28th shows very little sign of atmospheric noise pollution. Interestingly though, if degassing was intensifying at the time generating stronger acoustic signals at 3–5 Hz, this did not have a noticeable effect on the seismic output of the low- or high-frequency range. This is different to what is observed at the beginning and end of the deployment when the increased acoustic amplitudes coincide with increased seismic amplitudes. These variations hint at a complex relationship between seismic output and acoustic emissions, which will be discussed in Section 7.

### *4.1. High-frequency tremor activity*

In Fig. 4.2 we look at the entire deployment duration highlighting the temporal evolution of the acoustic spectrum in panel (a) as well as all incidences of high-frequency seismic tremor (panel b). Tremor episodes are present particularly in the first few hours of the deployment, followed by quieter periods before activity increased again during the later parts of the deployment as observed in Fig. 4.1. During the periods of interest analysed in detail in Figs. 5.1, 5.3, and 5.4 — indicated by vertical red lines — the first interval, which occurred early in the deployment, exhibits a much stronger acoustic signal in the 3–5 Hz range than the later interval.

## 5. Characterizing episodic high-frequency tremor

During the six day-long deployment of short-period instruments we manually detected about 50 short-duration episodes of high-frequency tremor within the 12–15 Hz band using the Spectral Width as seen in Figs. 3.1 and 4.2 ranging between several minutes to over half an hour. While Cannata et al. (2010), Heleno et al. (2006), Matoza and Fee (2014) or Reiss et al. (2023) report on volcanic tremor observed $> 10$ Hz on different volcanoes, tremor recorded at such high frequencies remains a rare observation. There are substantial differences between the tremor signals described in Cannata et al. (2010), which have a repetitive nature and stable durations, and the high-frequency tremor that we observe; our high-frequency tremor signals do not exhibit repetitive behaviour and have variable durations. Heleno et al. (2006) discuss harmonic tremor showing regularly spaced spectral bands which we also do not observe.

Below, we will investigate examples of high-frequency tremor in more detail looking into three tremor episodes within the highlighted parts in Fig. 4.1 that showcase the complexity and variability of these signals at Mt. Etna.

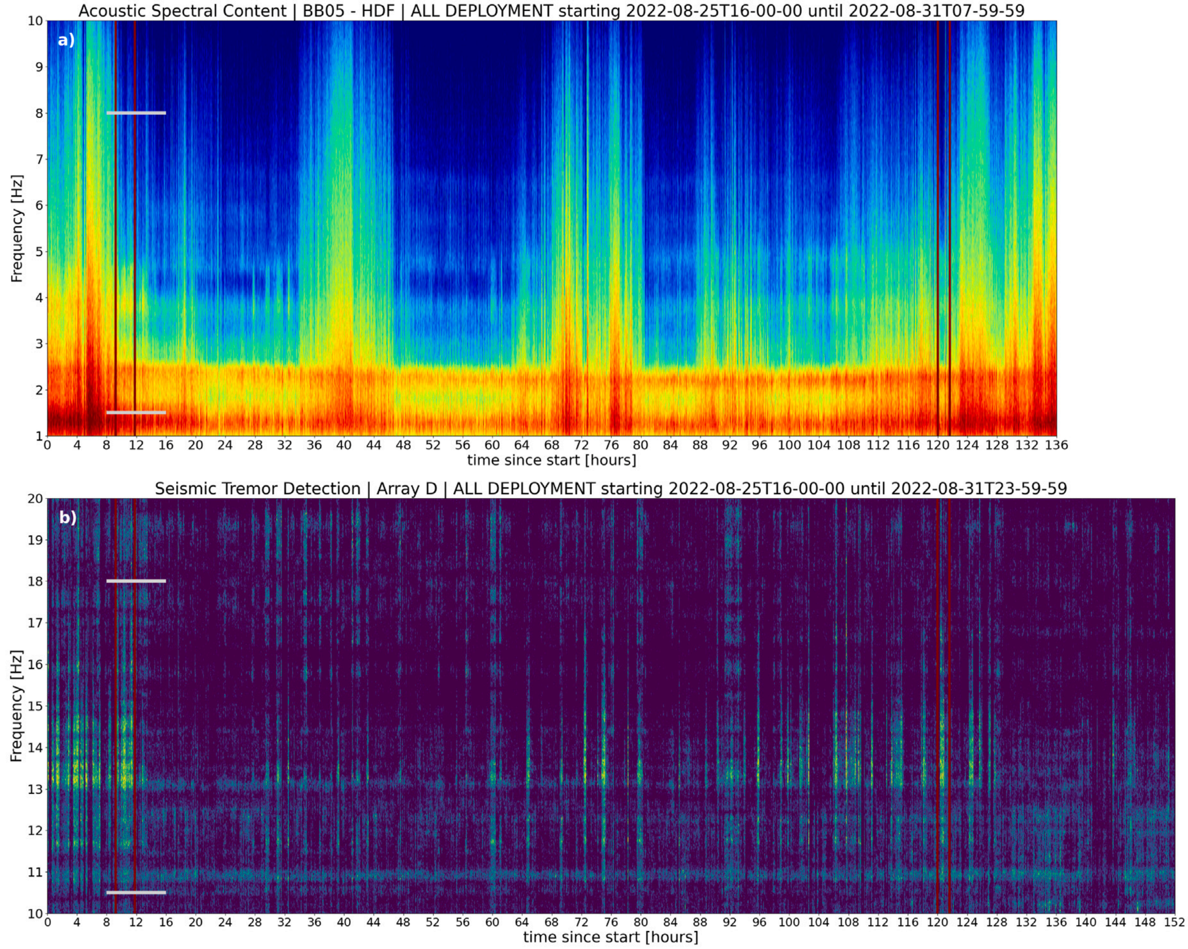

**Fig. 4.2.** Overview of the acoustic spectral evolution across the entire deployment period (panel (a)) as well as high-frequency seismic tremor activity (panel (b)) calculating the spectral width using COVSEISNET as above in Fig. 3.1. The tremor episodes closely investigated in Figs. 5.1, 5.3 and 5.4 are marked by vertical red lines. The 8-hour window seen in Fig. 3.1 is highlighted by horizontal grey lines.

### 5.1. *Case 1: High-frequency seismic tremor accompanied by acoustic signal across various frequency bands*

The first example, shown in Fig. 5.1, presents an episode of high-frequency tremor recorded between 03:00 and 04:00 UTC on 26 August during the deployment period. Panel (b) shows waveform coherency computed across all stations in Array D using the COVSEISNET tremor detection tool (Seydoux et al., 2016 and Soubestre et al., 2018), as previously introduced in Fig. 3.1.

The tremor band between 12–15 Hz is clearly variable in intensity and is strongest during the interval from approximately 3 to 28 min into the one-hour period. Adjacent frequency bands also show a slight increase in coherent signal content compared to the uncorrelated background noise. This 12–15 Hz tremor band dominates the amplitude spectrum, with a prominent spectral peak around 14 Hz visible in Panel (a). Additionally, both Panels (a) and (b) capture the presence of the characteristic “Etna tremor” between 1–5 Hz, which reaches substantially higher amplitudes (refer to displacement axes in Panels (e) and (g) for high- and low-frequency ranges, respectively).

High-frequency tremor is also apparent in Panel (e), where the seismic envelopes decrease significantly in tandem with the drop in coherent energy detected in Panel (b). The envelopes are calculated using 120-second windows with a two-thirds overlap, applying the median to suppress impulsive events from degassing craters BNC and SEC.

Panel (a) further highlights the strong attenuation of high-frequency content over short distances, particularly in heterogeneous environments such as volcanic edifices. The thin blue lines in the spectrum represent the 16 individual stations of Array D and illustrate a wide spread in amplitudes — ranging from 15 to 60 nm Panel (e) — at around 8 min into the time window, despite an array aperture of only 80$m$.

Panels (c) and (d) show the acoustic spectral content at station BB05 and its temporal evolution, respectively. Three prominent spectral peaks are visible at 1.3, 2.2, and 3.8 Hz. Notably, the 3.8 Hz peak in Panel (d) shows a striking similarity in its temporal evolution to the high-frequency seismic tremor in Panel (b): it is weak at first, intensifies after minute 3, and then fades after minute 28.

To highlight this similarity, the cumulative trends for the relevant frequency bands are shown in Panel (f), after zero-meaning and normalization by standard deviation. The seismic content filtered at 12–15 Hz (dashed bright blue line) and the acoustic band at 3.4–5 Hz (solid orange line) show nearly identical trends, supporting the visual impression from Panels (b) and (d) and suggesting a correlation between the two signals. It should be noted here though that, even other acoustic bands — including 12–15 Hz, where the seismic tremor is found — exhibit similar cumulative trends in this example.

The most striking observation is that the frequency ranges of these temporally correlated seismic and acoustic signals differ: 12–15 Hz (seismic) versus 3–5 Hz (acoustic). This suggests that low-frequency acoustic emissions may be linked to the high-frequency seismic tremor through a simultaneous driving process, as inferred from the shared amplitude trends over time. Additionally, a potential connection to low-frequency seismic tremor cannot be excluded, given the similarities in cumulative trends shown in Panel (h).

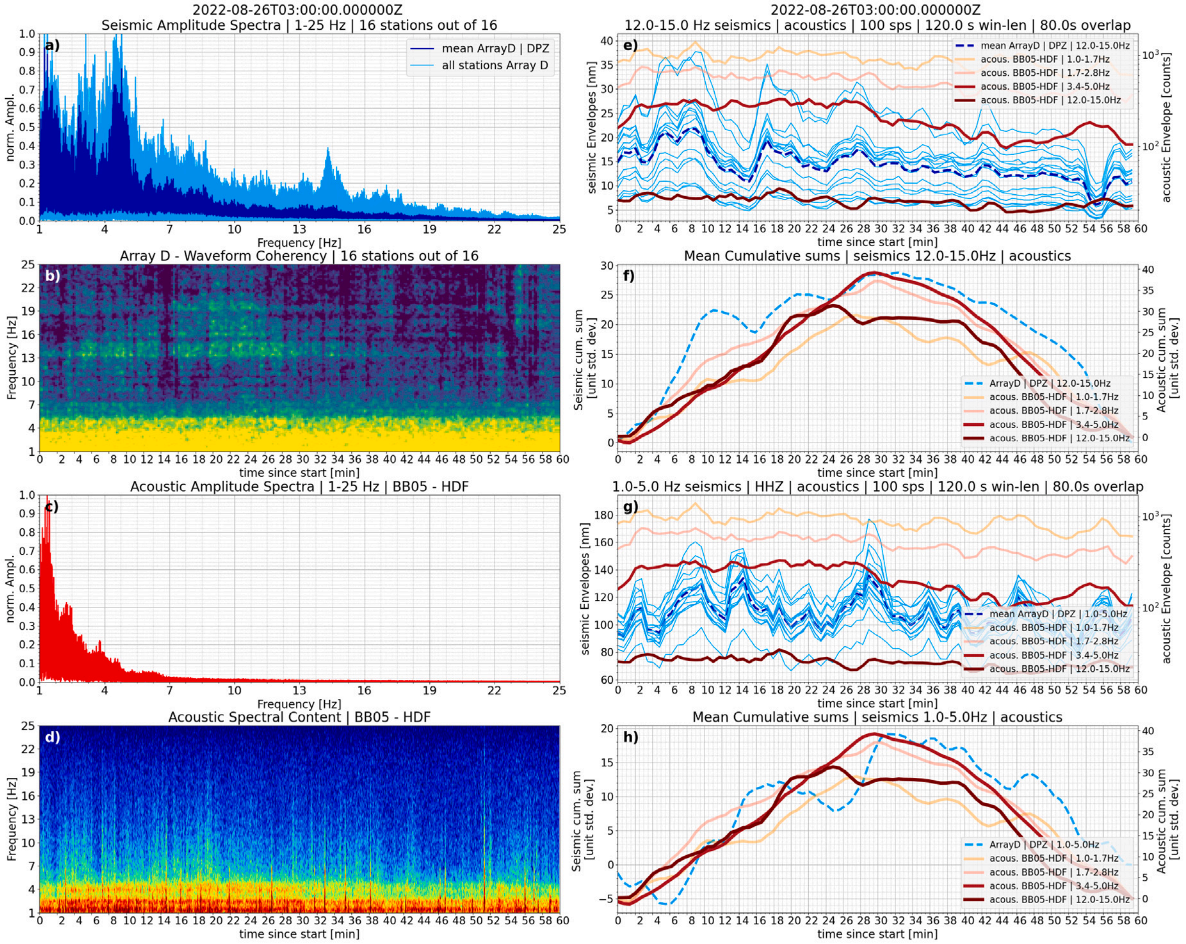

**Fig. 5.1.** Detailed overview of a one-hour long record of data including an episode of high-frequency tremor, including spectral, amplitude, and trend analysis in both time and frequency domains. Panels (a) and (b) show the seismic spectra and waveform coherency-based tremor detection (spectral width), respectively. Acoustic spectral content is displayed in panels (c) and (d). Panels (e)–(h) present the temporal evolution of amplitude envelopes and cumulative trends across various frequency bands. In panel (e), the thin solid bright blue lines represent individual stations from Array D (comprising 16 stations). All panels (e)–(h) use dual y-axes: the left *y*-axis corresponds to seismic data, and the right *y*-axis to acoustic data. This figure layout is consistent with the subsequent case studies shown in Figs. 5.3 and 5.4.

A key question arises: How can this close temporal match between high-frequency seismic tremor and low-frequency acoustic signals be explained? Given the distinct frequency ranges, it is likely that the two signals are generated by separate processes that are nonetheless linked due to their match in time. A non-linear transition of energy from air to solid medium causing a frequency shift can be ruled out, as helicopter-produced signals are consistently recovered on both acoustic and seismic channels at the same expected frequencies (see Fig. 5.2). Similar to the findings of Eibl et al. (2015), we observe gliding acoustic tremor patches and associated overtones from helicopters flying over the volcano, particularly in the morning and afternoon. The coherence in panels (d) and (e) clearly demonstrates that acoustic signals are coupled into the ground without a frequency shift.

### 5.2. Case 2: High-frequency tremor episode matched well by 3–5 Hz acoustic band

This case investigates the strongest high-frequency tremor episode recorded between 02:00 and 03:00 UTC on 26 August (Fig. 5.3). Coherent tremor energy, primarily within the 12–15 Hz band, is detected throughout the entire one-hour period, with maximum intensity observed between minutes 13 and 36, as shown in Panel (b) and confirmed by the amplitude envelopes in Panel (e) as well as the cumulative trend in Panel (f). The spectral peak near 14 Hz, shown in Panel (a), is the most prominent across all cases examined.

Three distinct spectral peaks in the acoustic signal — at approximately 1.3 Hz, 2.2 Hz, and 3.8 Hz — are clearly visible again in Panel (c), similar to Case 1. Additionally, the 3–5 Hz acoustic band is strongly expressed in the acoustic spectrogram (Panel (d)) and exhibits a temporal evolution that closely matches the high-frequency seismic tremor observed in Panel (b).

Given that this episode occurred only one hour prior to the one analysed in Case 1, it is not surprising that the key observations are largely consistent between the two cases. The cumulative trends for the 12–15 Hz seismic band and the 3–5 Hz acoustic band (Panel (f)) align closely during the interval of strongest tremor activity. This example and Case 1 taken together, these observations strongly support the interpretation that high-frequency seismic tremor and low-frequency acoustic signals are generated by separate, but temporally linked, physical processes.

However, in contrast to Case 1, the trends diverge more significantly outside this period. Notably, the other acoustic bands show far less agreement with the seismic trend, and the 12–15 Hz acoustic band in particular behaves quite differently from its seismic counterpart indicating no direct air-to-ground coupling in this frequency range. This reinforces the interpretation that the strongest correlation exists specifically between the 12–15 Hz seismic band and the 3–5 Hz acoustic band.

Unlike in Case 1, the low-frequency seismic cumulative trend ($<$ 5 Hz) deviates more clearly from the high-frequency seismic tremor

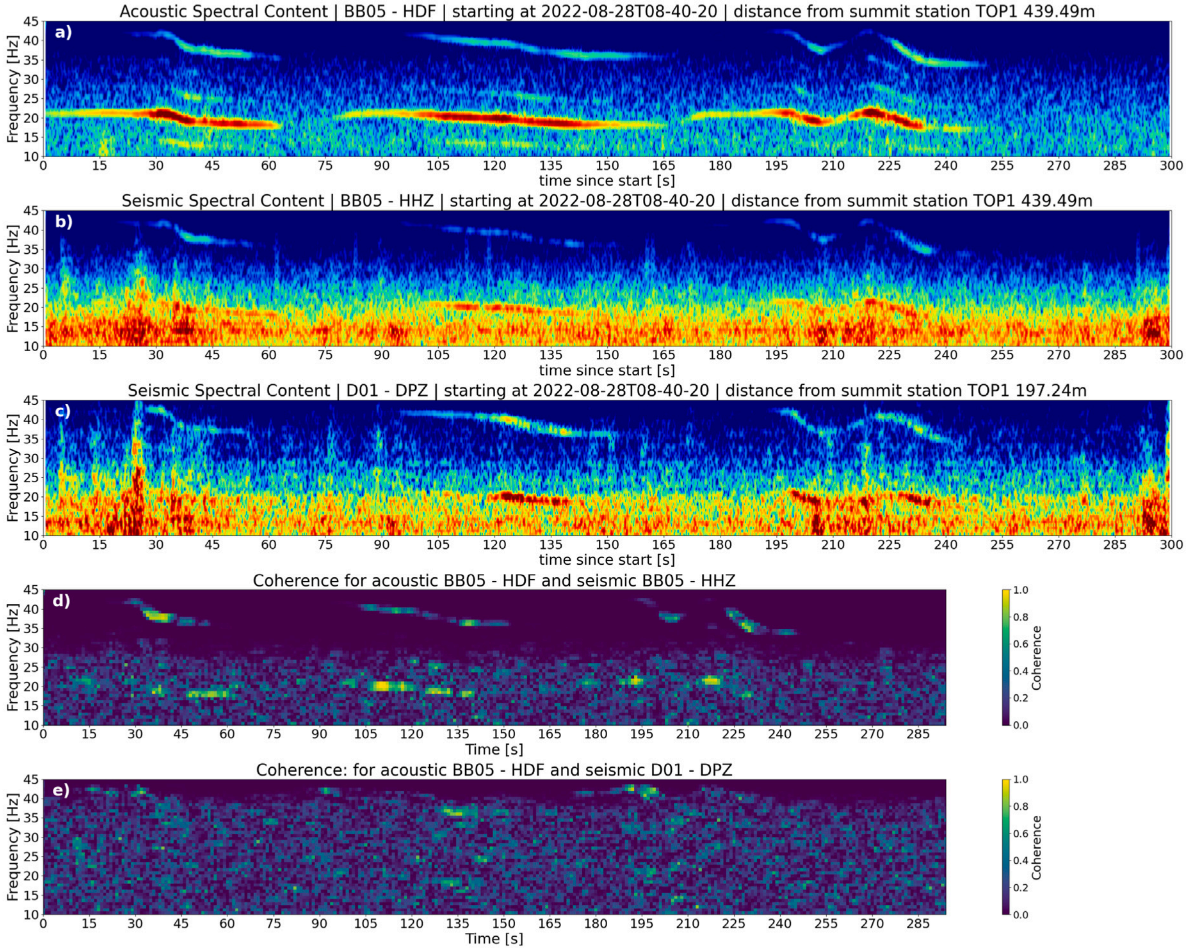

**Fig. 5.2.** Gliding tremor observed from a helicopter passing over the summit of Mt. Etna. Panel (a) shows the acoustic spectrum, clearly revealing both the fundamental frequency and its overtones. The data is filtered between 10–45 Hz, highlighting the helicopter-induced gliding tremor at consistent frequencies. The signal is also seen at a different short-period seismic station, as shown in Panel (c). Distances from the summit reference station (BNC) are indicated in the titles of the respective panels. In panels (d) and (e) the coherence spectrogram is found between the acoustic data from panel (a) and seismic data from panel (b) (same station) and the acoustic data from panel (a) and seismic data from panel (c) (different station), respectively.

in this case, suggesting that the typical Etna tremor and these high-frequency signals may be driven by separate processes.

### *5.3. Case 3: High-frequency seismic tremor not matched by acoustic signal*

This final case study examines the one-hour interval between 16:00 and 17:00 UTC on 30 August (Fig. 5.4). It captures another strong high-frequency tremor episode, beginning around minute 21 and lasting for over half an hour. The episode is clearly visible in Panel (b) and the seismic amplitude envelopes Panel (e). As in previous cases, adjacent frequency bands also exhibit increased coherent energy, and a prominent spectral peak is again observed near 14 Hz Panel (a).

However, this example displays a notable deviation from Cases 1 and 2. Specifically, the 3–5 Hz acoustic band — previously well-expressed — is largely absent here. No distinct peak is observed in the acoustic spectrum Panel (c), and the spectrogram Panel (d) shows no significant energy in this band during the high-frequency seismic tremor. Importantly, the seismic amplitude of this episode is comparable to that of Case 1, suggesting that the absence of the 3–5 Hz acoustic signature cannot be attributed to a weaker tremor (see Panel (e) and compare with Fig. 5.1).

As a result, the cumulative trend of the 12–15 Hz seismic band diverges markedly from that of the 3–5 Hz acoustic band, and no other acoustic band shows a matching trend either Panel (f). Additionally, the low-frequency seismic content (< 5 Hz), typically associated with Etna tremor, exhibits an opposing trend, further indicating a decoupling of low- and high-frequency components in this case.

The absence of the 3–5 Hz acoustic signal — previously interpreted as a likely indicator of degassing activity (Fee et al., 2010) — suggests that the process generating this acoustic emission may not be essential for the occurrence of high-frequency tremor. This raises the possibility that in this case, the tremor may be triggered independently of degassing, which therefore may not be directly involved in the seismic signature of the tremor.

As noted in Case 1, the acoustic signature of a helicopter overflight is also present in this episode Panel (d), visible between 18 and 22 Hz from minutes 36 to 41. Additionally, a faint indication of a secondary gliding tremor patch appears near 14 Hz at approximately minute 36, possibly related to the same overflight event.

## 6. Variability of seismic-acoustic correlations

As shown in the previous case studies, a potential seismic–acoustic correlation between the 12–15 Hz seismic tremor and the 3–5 Hz acoustic signal can be observed, but it is not consistent across all examples. To better illustrate the complexity and variability encountered when jointly analysing the seismic and acoustic data, we plot the median seismic and acoustic amplitudes of 10-minute non-overlapping time windows for the frequency bands of interest against one another (Fig. 6.1).

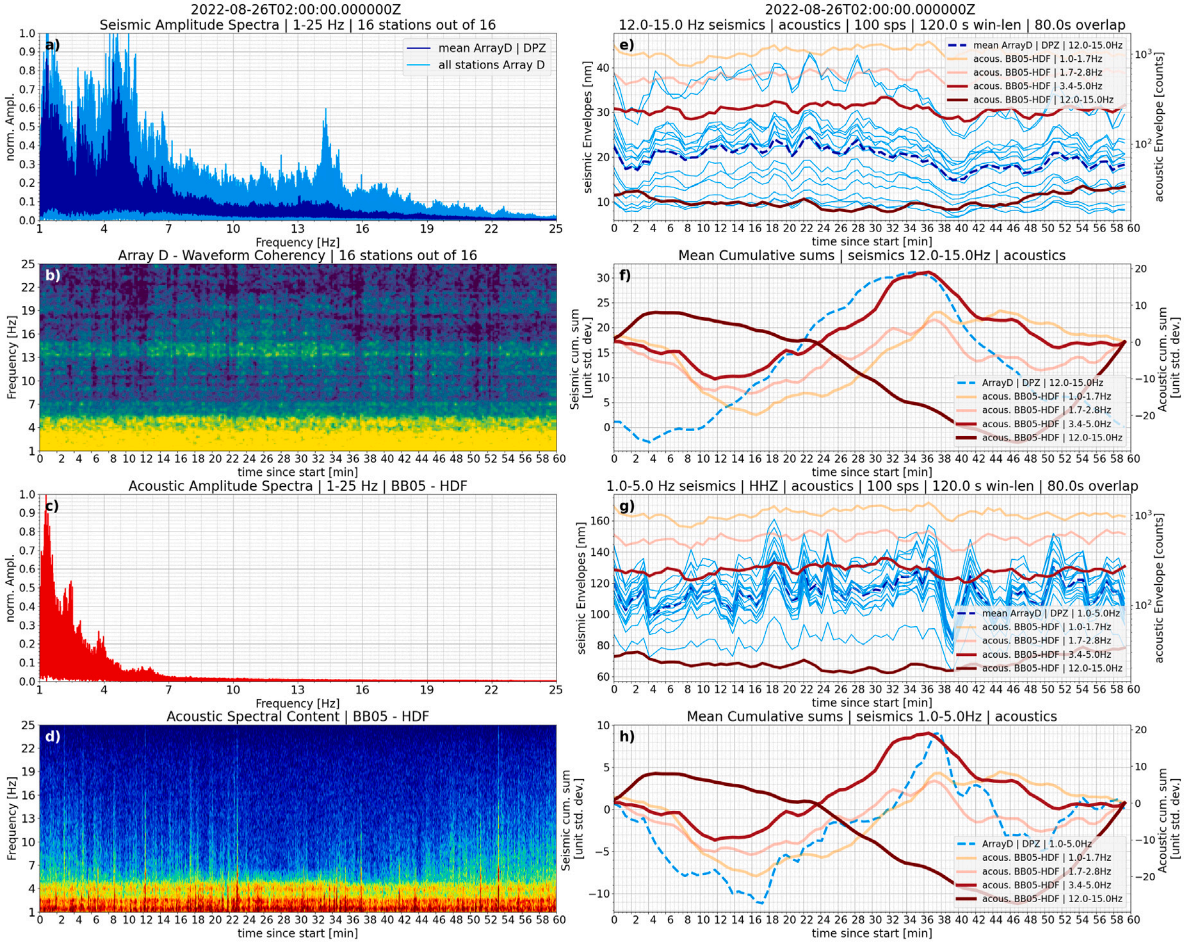

**Fig. 5.3.** Detailed overview of a second 1-hour long record of data including an episode of high-frequency tremor.

Panel (a) displays the relationship between the 12–15 Hz seismic tremor and the 3–5 Hz acoustic signal, with acoustic amplitudes plotted as a function of seismic amplitudes. Overall, the correlation is weak, revealing considerable variability in acoustic energy for any given level of seismic activity, and vice versa. Nonetheless, a broad trend towards higher amplitudes in one signal when the other increases can be observed. However, this relationship is loose and not necessarily valid for individual cases — such as Case 3 — highlighted here by the wide spread in the data. Most time windows fall within a relatively narrow range of seismic amplitudes (7–15 nm), while the corresponding acoustic amplitudes range from 20 to over 400 counts, a variation by more than a factor of 20.

As previously mentioned, atmospheric conditions such as wind or rainfall influence the acoustic spectral content. To account for this, Panel (d) compares the 3–5 Hz acoustic band with a broader high-frequency acoustic band (15–30 Hz), which is more sensitive to wind-induced noise. The distribution shows that time windows with 3–5 Hz acoustic amplitudes below ∼ 30 counts are generally unaffected by atmospheric disturbances, as these coincide with low amplitudes in the 15–30 Hz band. In contrast, higher-amplitude outliers in the 3–5 Hz band are often accompanied by elevated energy in the 15–30 Hz range, suggesting an atmospheric origin. Assuming that the 3–5 Hz acoustic amplitudes in the 25–300 count range are primarily volcanic in origin, the data indicate that high-frequency seismic tremor may be triggered under a range of conditions. As illustrated in Case 3 (Fig. 5.4), strong high-frequency tremor may occur with minimal accompanying acoustic energy, potentially implying weak or absent degassing during such events as previous findings have linked continuous degassing to low-frequency acoustic tremor (Fee et al., 2010).

Panel (b) shows no evidence of a systematic correlation between the 12–15 Hz seismic and 12–15 Hz acoustic bands, further supporting the idea that this frequency range is not directly coupled in the acoustic domain.

In Panel (c), a weak positive correlation is observed between the low-frequency (< 5 Hz) and high-frequency (12–15 Hz) seismic bands. However, the wide variation in amplitude ratios across the dataset suggests the absence of a simple linear relationship when analysing short time windows. Nevertheless, a broader long-term correlation may exist, as suggested by the trends observed in Fig. 4.1.

## 7. Volcanic tremor's driving mechanisms

The above exemplifications form a picture of quite convoluted high-frequency tremor signals, which show a complex seismic-acoustic ratio and temporal evolution. The recovery of volcanic tremor at such high frequencies is a rare finding in itself with very few exceptions like Cannata et al. (2010) or Heleno et al. (2006) reporting on high-frequency tremor signals. Our findings here suggest that the high-frequency tremor may be generated under different circumstances as we see some tremor episodes exhibiting a high seismic-acoustic correlation but also recover specific tremor episodes which are lacking the correlation with acoustic data expected for tremor directly related to degassing (see Fig. 5.4). Moreover, the observed high-frequency tremor is seemingly identical in spectral characteristics and energy output regardless of the changing acoustic record. Interestingly, those examples of correlating seismic and acoustic data show different frequencies indicating two potential processes driving these signals which are likely linked due to their match in time.

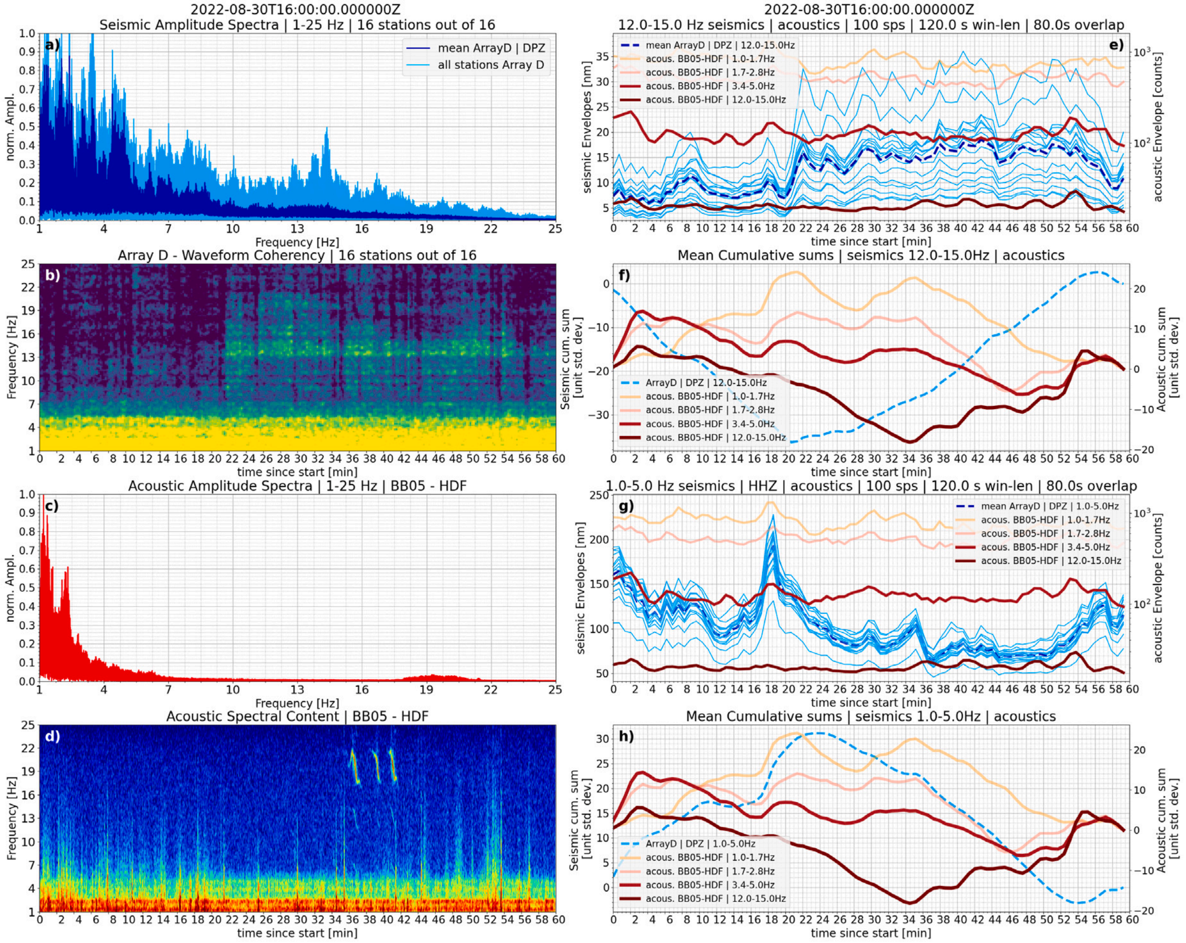

**Fig. 5.4.** Detailed overview of a third episode of high-frequency tremor (1 h of data). Here, the accompanying acoustic signal at 3–5 Hz observed before is largely missing.

### 7.1. Established models for volcanic tremor

Traditionally, the generation of volcanic tremor is attributed to processes involving mass transport (magma flow in volcanic conduits) as described in Steinberg and Steinberg (1975) or Neuberg and Pointer (2000). This link makes tremor a promising candidate for identifying and characterizing unrest and forecasting eruptions at volcanoes.

A widely accepted source mechanism for volcanic tremor is sustained degassing activity (e.g., Williams-Jones et al. (2001), Konstantinou and Schlindwein (2002)). Clear links have been demonstrated between persistent degassing and variable tremor amplitude at Mt. Etna in previous studies (e.g., Gresta et al. (1991), Zuccarello et al. (2013)). Seismic tremor at Mt. Etna is widely observed to frequently precede and accompany eruptive activity (Cannata et al., 2008), confirming its potential use in eruption forecasting. Leonardi et al. (2000), found that the correlation between the tremor amplitude and the $SO_2$ flux rates reaches its maximum during eruptive periods. The style of eruption has been shown to influence the characteristics of tremor signals (Cannata et al., 2018). Fee et al. (2010) identified persistent acoustic tremor associated with continuous volcanic degassing, attributing variations in tremor energy to resonance within gas-filled cavities and to fluctuations in degassing intensity. Despite numerous studies linking tremor to magma or gas movement, these models fail to explain the observed range of tremor signals and their relation to other monitoring parameters. Aiuppa et al. (2009), for example, showed an inverse correlation between $CO_2$ flux rates and tremor recorded at Stromboli; Cannata et al. (2009), on the other hand, observed a time-lagged correlation between those parameters at Mt. Etna with tremor lagging behind degassing by about 50 days. Young et al. (2003) report the opposite at Soufriere Hills Volcano, Montserrat (WI), where gas flux lags behind tremor.

### 7.2. Non-fluid related driving mechanisms

One aspect is common to many of the models - they require the presence of fluids (magma, gases) involved in the processes that generate tremor. Several recent studies have challenged this hypothesis.

Bean et al. (2013) demonstrated how seismicity of tremor-like character could be generated without invoking the presence of fluids at the source. The authors conduct numerical simulations for very low-cohesian and weak materials common on a volcanic edifices (e.g., Apuani et al. (2005) who studied deposits from Stromboli's upper edifice). The numerical simulations carried out are based on a model developed by Amitrano (2003) and they find that breaching a certain stress threshold leads to the continuous generation of low-amplitude, very small stress-drop seismic events so closely spaced in time that they appear as tremor and are related to a diffusive failure pattern. This observation is in agreement with the numerical results of Amitrano (2003) who studied the seismic output associated with changing angles of internal friction. On key finding is, that the seismic b-value of material of low angles of internal friction exhibits non-power-law scaling lacking larger events.

Very similar results are seen for a Long-Period (LP) seismicity catalogue from Mt. Etna acquired by Bean et al. (2013) suggesting that the weak material making up the upper edifice is found near the brittle-ductile boundary. This merely supports low-amplitude seismicity

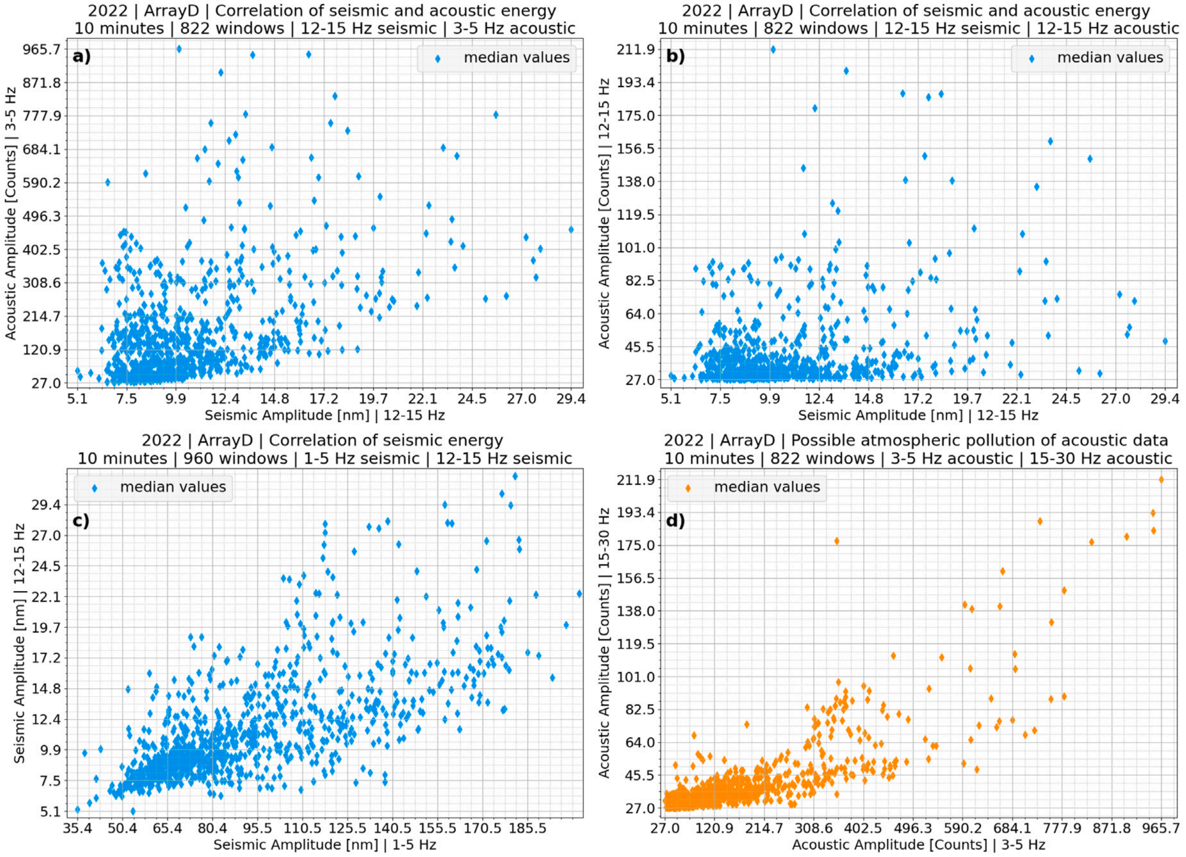

**Fig. 6.1.** Median amplitudes calculated over 10-minute non-overlapping windows for selected frequency bands of interest. Panel (a) shows a scatter plot of the 3–5 Hz acoustic band versus the 12–15 Hz seismic band, using all available data from the large deployment between 25 August and 1 September. For comparison, Panel (b) plots the 12–15 Hz acoustic band as a function of the high-frequency (12–15 Hz) seismic tremor. Panel (c) compares the typical low-frequency Etna tremor (< 5 Hz) with the high-frequency tremor. Panel (d) evaluates the influence of atmospheric conditions on the acoustic data, highlighting potential weather-related variability.

merging into tremor due to diffusively damaged material across the edifice rather than localized ruptures as the weak material cannot sustain the required stress for larger events. Bean et al. (2013) therefore propose that the swarms of LP events on Mt. Etna can be caused by quasi-brittle behaviour, as very small stress-drop events are triggered by deformation, that the edifice undergoes. Crucially, they point out that even if changes in stress levels occurring are contributed to by gas influx or magma migration, the failure process itself can be dry mechanical.

This concept is supported by laboratory experiments carried out by Rowley et al. (2021) who encounter tremor-like acoustic emissions from a sample of Napolitan Tuff under slow compression after having been fully dried. Despite the complete absence of fluids, tremor-like signals are recovered and the associated damage pattern is diffusive in character rather than localized.

### *7.3. Driving mechanisms of high frequency tremor in recorded signals?*

The varying seismo-acoustic amplitude ratios observed in the different high-frequency tremor episodes clearly suggest that the tremor is triggered under various circumstances and thus a model linking the tremor directly to degassing is not sufficient to explain all incidences of tremor detected. Based on the numerical work by Amitrano (2003) as well as findings by Rowley et al. (2021) from laboratory tests on typical volcanic material we suggest a non-fluid related source mechanism needs to be considered here. As proposed by Bean et al. (2013) the weak material with low angles of internal friction that the edifice is made up of may generate low-amplitude, tremor-train like signals due to quasi-brittle failure. Similar ideas for tremor signals composed of many individual events are considered by Dmitrieva et al. (2013) investigating tremor signals as the result of discrete events occurring in rapid succession or (Hotovec et al., 2013) finding that superimposed earthquakes shape a tremor-like signal when occurring increasingly rapidly. We suggest a similar process may be causing these tremor episodes here at a smaller scale and thus higher frequency. The tremor found in a high frequency band is suggestive of mesoscale brittle failure that may generate a cascade of low amplitude low stress drop events that merge into tremor.

A key aspect to consider here are the different frequency bands for the high-frequency seismic tremor at 12–15 Hz and the correlating acoustic signal which primarily dominates at 3–5 Hz. As we have shown we do not expect any non-linear coupling of acoustic signals into solid medium towards higher frequencies as the acoustic helicopter signals are retrieved without any frequency shift in the seismic data similar to observations made by Eibl et al. (2015). Such coupling has also been investigated by Matoza and Fee (2014) who find seismic tremor that is the result of air-to-ground coupling rather than an independent subsurface source. Therefore, we conclude that the observed different frequencies for the seismic and acoustic signals in question here are almost certainly the result of two different processes which, however, are tied together through their temporal match observed for instance in Figs. 5.1 and 5.3. We propose that continuous passive degassing causes the 3–5 Hz acoustic signal (similar to Fee et al. (2010) linking oscillation of gases in cracks to acoustic tremor) while the escaping gases produce very small stress changes sufficient to trigger quasi-brittle failure of the very weak host rock which is picked up at 12–15 Hz in the seismic data. However, considering the before mentioned examples of tremor lacking the acoustic correlation quasi-brittle failure may even be triggered without degassing present. Instead non-fluid related processes such as gravitational load as discussed by Bean et al. (2013) may be a potential driver. Furthermore, the edifice is subject to a highly complex and varying stress field causing ongoing slow deformation (Pezzo et al., 2023), which may provide the necessary small stress level changes to generate diffusive failure in weak material. The possibility for this has been demonstrated by Rowley et al. (2021) producing tremor signals from volcanic material in entirely dry conditions. We want to point out though that subsurface fluid migration (e.g. gas accumulations) may still occur when acoustic signatures are absent - degassing may still indirectly drive the high-frequency seismic tremor in those incidences.

To shed more light onto tremor possibly being purely deformation driven without a direct link to fluids further investigations are required, e.g. focussing on the source locations of the tremor episodes. Tremor's source location may help in gaining better understanding of underlying processes as seen in previous studies such as Almendros et al. (2014), Yukutake et al. (2017), Leva et al. (2022) who are able to link tremor to degassing processes or hydrothermal systems based on its source location. Following the discussion above, we expect tremor that is not directly linked to degassing to be more diffuse rather than localized in nature. Its source regions would therefore not necessarily be confined to the degassing crater area, but could instead be distributed more broadly across the volcanic edifice.

## 8. Conclusion

We present a seismo-acoustic data set from the summit region of Mt. Etna containing rarely observed high-frequency short-duration episodes of tremor dominating in the 12–15 Hz band. These tremor signals are found to show significantly varying seismic-acoustic amplitude ratios suggesting that different circumstances may lead to the triggering of high-frequency tremor. Therefore, degassing activity may not be sufficient to explain all of its occurring incidences. We propose that quasi-brittle, mesoscale failure of very weak material in the summit region may need to be considered as the direct source mechanism of the episodic tremor as suggested by several previous studies. Some of the high-frequency tremor seems to be indirectly driven by continuous degassing activity producing a time-matching acoustic signal at a different frequency. On the other hand, we find examples lacking the accompanying acoustic signal, potentially indicating degassing (and therefore involved fluids) is not required as a triggering process as it appears to be absent at the time. It cannot be ruled out though, that subsurface fluid migration still occurs causing small stress level changes ultimately leading to material damage producing high-frequency seismic tremor while gases are unable to escape and therefore do not leave an acoustic signature. Interestingly, though, even if degassing indirectly triggers the seismic tremor, the actual source mechanism producing the seismic tremor signal may be dry mechanically to account for the different frequency at which the seismic tremor is observed as opposed to the acoustic signal. We are currently conducting further investigations into tremor source locations, to improve our understanding of the phenomenon.

## CRediT authorship contribution statement

**Maurice Weber:** Writing – review & editing, Writing – original draft, Visualization, Formal analysis, Data curation, Conceptualization. **Christopher J. Bean:** Writing – review & editing, Supervision, Funding acquisition, Conceptualization. **Ivan Lokmer:** Writing – review & editing, Supervision. **Silvio De Angelis:** Writing – review & editing. **Luciano Zuccarello:** Writing – review & editing.

## Declaration of competing interest

The authors declare that they have no known competing financial interests or personal relationships that could have appeared to influence the work reported in this paper.

## Acknowledgements

We want to thank the IMPROVE European Horizon‘s 2020 research and innovation programme under which the fieldwork acquiring this data was carried out. Furthermore, we would like to thank numerous people for helping during the field campaigns to Mount Etna in summer 2022 who are Vittorio Minio, Elisabeth Glueck, Regina Maass and Eleanor Dunn. Also, we want to thank Ka Lok Li for assisting with the design of the array configurations. Thanks are also due to the following two projects: "Progetto INGV Pianeta Dinamico" -Subproject VT-DYNAMO 2023- code CUP D53J19000170001 - which was funded by Italian Ministry MIUR ("Fondo Finalizzato al rilancio degli investimenti delle amministrazioni centrali dello Stato e allo sviluppo del Paese", legge 145/2018) as well as SINFONIA2, progetto Bando Ricerca Libera 2024- Delibera 56/2025-INGV.

## Data availability

Data will be made available on request.

## References

Aiuppa, A., Burton, M., Caltabiano, T., Ripepe, M., 2009. Anti-correlation between gas flux and volcanic tremor on stromboli volcano. EGU Gen. Assem. 2009 13671.

Almendros, J., Abella, R., Mora, M.M., Lesage, P., 2014. Array analysis of the seismic wavefield of long-period events and volcanic tremor at arenal volcano, costa rica. J. Geophys. Res.: Solid Earth 119, 5536–5559.

Amitrano, D., 2003. Brittle-ductile transition and associated seismicity: Experimental and numerical studies and relationships with the b value. J. Geophys. Res. 108, 2044—-2059.

Apuani, T., Corazzato, C., Cancelli, A., Tibaldi, A., 2005. Physical and mechanical properties of rock masses at stromboli: A dataset for volcano instability evaluation. Bull. Eng. Geol. Env. 64, 419–431.

Bean, C.J., Barros, L.D., Lokmer, I., Métaxian, J.P., Brien, G.O., Murphy, S., 2013. Long-period seismicity in the shallow volcanic edifice formed from slow-rupture earthquakes. Nat. Geosci. 7, 71–75.

Cannata, A., Catania, A., Alparone, S., Gresta, S., 2008. Volcanic tremor at mt. Etna: inferences on magma dynamics during effusive and explosive activity. J. Volcanol. Geotherm. Res. 178, 19–31.

Cannata, A., Di Grazia, G., Giuffrida, M., Gresta, S., Palano, M., Sciotto, M., 2018. Space- time evolution of magma storage and transfer at mt. Etna volcano (Italy): the 2015/2016 reawakening of voragine crater. Geochem. Geophys. Geosys. 19, 471–495.

Cannata, A., Di Grazia, G., Montalto, P., Ferrari, F., Nunnari, G., Patanè, D., Privitera, E., 2010. New insights into banded tremor from the 2008–2009 mount etna eruption. J. Geophys. Res.: Solid Earth 115.

Cannata, A., Giudice, G., Guerrieri, S., Montalto, P., Alparone, S., et al., G.D., 2009. Relationship between soil CO2 flux and volcanic tremor at mt. Etna: implications for magma dynamics. Env. Earth Sci. 61, 477–489.

Chardot, L., Jolly, A.D., Kennedy, B.M., Fournier, N., Sherburn, S., 2015. Using volcanic tremor for eruption forecasting at white island volcano (whakaari), New Zealand. J. Volcanol. Geotherm. Res. 302, 11–23.

Di Lieto, B., Saccorotti, G., Zuccarello, L., Rocca, M.L., Scarpa, R., 2007. Continuous tracking of volcanic tremor at mount etna, Italy. Geophys. J. Int. 169, 699–705.

Dmitrieva, K., Hotovec-Ellis, A.J., Prejean, S., Dunham, E.M., 2013. Frictional-faulting model for harmonic tremor before redoubt volcano eruptions. Nat. Geosci. 6, 652–656.

Eibl, E.P.S., Lokmer, I., Bean, C.J., Akerlie, E., Vogfjörd, K.S., 2015. Helicopter vs. Volcanic tremor: Characteristic features of seismic harmonic tremor on volcanoes. J. Volcanol. Geotherm. Res. 304, 108–117.

Fee, D., Garcés, M., Patrick, M., Chouet, B., Dawson, P., Swanson, D., 2010. Infrasonic harmonic tremor and degassing bursts from halema'uma'u crater, kilauea volcano, hawaii. J. Geophys. Res. 115, B11316.

Ganci, G., Cappello, A., Neri, M., 2023. Data fusion for satellite-derived earth surface: The 2021 topographic map of etna volcano. Remote. Sens. 15.

Gresta, S., Montalto, A., Patanè, G., 1991. Volcanic tremor at mount etna (january 1984–march 1985): its relationship to the eruptive activity and modelling of the summit feeding system. Bull. Volcanol. 53, 309–320.

Heleno, S.I., Faria, B.V., Bandomo, Z., Fonseca, J.F., 2006. Observations of high-frequency harmonic tremor in fogo, cape verde islands. J. Volcanol. Geotherm. Res. 158, 361–379.

Hotovec, A.J., Prejean, S.G., Vidale, J.E., Gomberg, J., 2013. Strongly gliding harmonic tremor during the 2009 eruption of redoubt volcano. J. Volcanol. Geotherm. Res. 259, 89–99.

Ibanez, J.M., Castro-Melgar, I., Cocina, O., Zuccarello, L., Branca, S., Pezzo, E.D., Prudencio, J., 2019. First 2-D intrinsic and scattering attenuation images of mt etna volcano and surrounding region from active seismic data. Geophys. J. Int. 220, 267–277.

Johnson, J.B., Aster, R., 2005. Relative partitioning of acoustic and seismic energy during strombolian eruptions. J. Volcanol. Geotherm. Res. 148, 334–354.

Konstantinou, K.I., Schlindwein, V., 2002. Nature, wavefield properties and source mechanism of volcanic tremor: a review. J. Volcanol. Geotherm. Res. 119, 161–187.

Leonardi, S., Gresta, S., Mulargia, F., 2000. Cross-correlation between tremor and SO2 flux data from mount etna volcano, 1987–1992. Phys. Chem. Earth 25, 737–740.

Leva, C., Rümpker, G., Wölbern, I., 2022. Multi-array analysis of volcano-seismic signals at fogo and brava, cape verde. Solid Earth 13, 1243–1258.

Matoza, R.S., Fee, D., 2014. Infrasonic component of volcano-seismic eruption tremor. Geophys. Res. Lett. 41, 1964–1970.

McNutt, S.R., 1992. Volcanic tremor. Encycl. Earth Syst. Sci. 4.

Neuberg, J., Pointer, T., 2000. Effects of volcano-topography on seismic broadband waveforms.. Geophys. J. Int. 143, 239–248.

Permana, T., Nishimura, T., Nakahara, H., Fujita, E., Ueda, H., 2019. Reliability evaluation of volcanic tremor source location determination using cross-correlation functions. Geophys. J. Int. 220, 1300–1315.

Pezzo, G., Palano, M., Beccaro, L., Tolomei, C., Albano, M., Atzori, S., Chiarabba, C., 2023. Coupling flank collapse and magma dynamics on stratovolcanoes: The mt. etna example from InSAR and GNSS observations. Remote. Sens. 15, 847.

Reiss, M.C., Massimetti, F., Laizer, A.S., Campus, A., Rümpker, G., Kazimoto, E.O., 2023. Overview of seismo-acoustic tremor at oldoinyo lengai, tanzania: Shallow storage and eruptions of carbonatite melt. J. Volcanol. Geotherm. Res. 442, 107898.

Rowley, P., Benson, P.M., Bean, C.J., 2021. Deformation-controlled long-period seismicity in low-cohesion volcanic sediments. Nat. Geosci. 14, 942–948.

Salerno, G.G., Burton, M., Di Grazia, G., Caltabiano, T., Oppenheimer, C., 2018. Coupling between magmatic degassing and volcanic tremor in basaltic volcanisms. Front. Earth Sci. 6.

Seydoux, L., Shapiro, N., de Rosny, J., Brenguier, F., Landes, M., 2016. Detecting seismic activity with a covariance matrix analysis of data recorded on seismic arrays. Geophys. J. Int. 204, 1430–1442.

Soubestre, J., Shapiro, N.M., Seydoux, L., de Rosny, J., Droznin, D.V., Droznina, S.Y., Senyukov, S.L., Gordeev, E.I., 2018. Network-based detection and classification of seismovolcanic tremors: Example from the klyuchevskoy volcanic group in kamchatka. J. Geophys. Res.: Solid Earth http://dx.doi.org/10.1002/2017JB014726.

Steinberg, G.S., Steinberg, A.S., 1975. On possible causes of volcanic tremor. J. Geophys. Res. http://dx.doi.org/10.1029/JB080i011p01600.

Tong, F., Seydoux, L., Journeau, C., Soubestre, J., 2024. Covseisnet python package. http://dx.doi.org/10.5281/Zenodo.10990032, Covseisnet/Covseisnet: Associate repository with a Zenodo DOI (1.0.0) [Software]. Zenodo.

Williams-Jones, G., Stix, J., Heiligmann, M., Barquero, J., Fernandez, E., Gonzalez, E.D., 2001. A model of degassing and seismicity at arenal volcano, costa rica.. J. Volcanol. Geotherm. Res. 108, 121–139.

Young, S.R., Voight, B., Duffell, H.J., 2003. Magma extrusion dynamics revealed by high- frequency gas monitoring at soufrière hills volcano, monserrat. Geol. Soc. Spec. Publ. 213, 219–230.

Yukutake, Y., Honda, R., Harada, M., Doke, R., Saito, T., Ueno, T., Sakai, S., Morita, Y., 2017. Analyzing the continuous volcanic tremors detected during the 2015 phreatic eruption of the hakone volcano. Springer Open Earth Planets Space http://dx.doi.org/10.1186/s40623-017-0751-y.

Zuccarello, L., Burton, M., Saccorotti, G., Bean, C., Patanè, D., 2013. The coupling between very long period seismic events, volcanic tremor, and degassing rates at mount etna volcano. J. Geophys. Res. Solid Earth 118, 4910–4921.